Controllable Disorder Engineering in Oxygen-Incorporated MoS$_2$ Ultrathin Nanosheets for Efficient Hydrogen Evolution

Junfeng Xie,[†] Jiajia Zhang,[†] Shuang Li,[†] Fabian Grote,[‡] Xiaodong Zhang,[†] Hao Zhang,[†] Ruoxing Wang,[†] Yong Lei,[‡] Bicai Pan,[†] and Yi Xie*[,†]

[†]Hefei National Laboratory for Physical Sciences at the Microscale, Department of Chemistry, University of Science and Technology of China, Hefei, Anhui 230026, People's Republic of China

[‡]Institute of Physics and IMN MacroNano (ZIK), Ilmenau University of Technology, Ilmenau, 98693, Germany

S Supporting Information

ABSTRACT: Molybdenum disulfide (MoS$_2$) has emerged as a promising electrocatalyst for catalyzing protons to hydrogen via the so-called hydrogen evolution reaction (HER). In order to enhance the HER activity, tremendous effort has been made to engineer MoS$_2$ catalysts with either more active sites or higher conductivity. However, at present, synergistically structural and electronic modulations for HER still remain challenging. In this work, we demonstrate the successfully synergistic regulations of both structural and electronic benefits by controllable disorder engineering and simultaneous oxygen incorporation in MoS$_2$ catalysts, leading to the dramatically enhanced HER activity. The disordered structure can offer abundant unsaturated sulfur atoms as active sites for HER, while the oxygen incorporation can effectively regulate the electronic structure and further improve the intrinsic conductivity. By means of controllable disorder engineering and oxygen incorporation, an optimized catalyst with a moderate degree of disorder was developed, exhibiting superior activity for electrocatalytic hydrogen evolution. In general, the optimized catalyst exhibits onset overpotential as low as 120 mV, accompanied by extremely large cathodic current density and excellent stability. This work will pave a new pathway for improving the electrocatalytic activity by synergistically structural and electronic modulations.
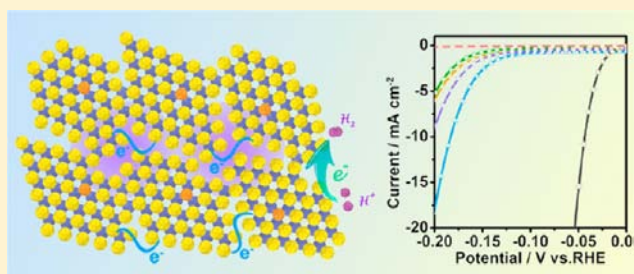
INTRODUCTION

Electrocatalytic hydrogen evolution reaction (HER) holds tremendous promise as an efficient and clean solution to face the energy crisis brought about by the severe consumption of traditional fossil fuels.[1−3] Although excellent HER performance has been reached for platinum and other precious metals,[4] replacing the expensive and rare catalysts with earth-abundant materials still attracts scientists' attention toward making the hydrogen production more economic and competitive.[5] During the past few years, many potential alternatives for platinum-based electrocatalysts have been exploited, including transition metal sulfides,[6−10] selenides,[11,12] borides,[13] carbides,[13,14] nitrides,[15] phosphides,[16] as well as a family of molecular catalysts.[17−19] Among all these alternatives, molybdenum disulfide (MoS$_2$) has received tremendous attention due to the earth-abundant composition and high activity, leading to the development of various kinds of MoS$_2$-based HER electrocatalysts in the form of crystalline[20−27] or amorphous states,[28−30] and even in molecular mimics.[31] As a typical transition-metal dichalcogenide (MX$_2$), where M represents a transition metal and X represents a chalcogen (S, Se, or Te), MoS$_2$ possesses a layered structure with weak van der Waals interactions between individual sandwiched S−Mo−S layers.[32−35] Owing to the anisotropic structure, MoS$_2$ is prone to form two-dimensional (2D) morphology that offers

large surface area and 2D permeable channels for ion adsorption and transport.[36−38] During the past few years, enormous effort has been made to clarify the HER mechanism of MoS$_2$-based electrocatalysts. Both theoretical[39] and experimental[23] studies concluded that the HER activity arises from the sites located along the edges of the 2D MoS$_2$ layers, while the basal surfaces are catalytically inert. That is, the unsaturated sulfur atoms on the edges play a crucial role in HER catalysis. Hence, increasing the number of unsaturated sulfur atoms is an efficient pathway to enhance the HER activity. Besides the aspect of active sites, the electric conductivity of catalysts is another crucial factor to affect the electrocatalytic activity because a high conductivity ensures a fast electron transport during the catalytic process.[40−43] Unfortunately, nanostructured MoS$_2$ exhibits poor intrinsic conductivity due to its large bandgap,[34] which significantly limits the overall HER rate.

On the basis of the above two key factors, enormous attempts have been made focusing on the improvement of either the number of active sites or conductivity of MoS$_2$ electrocatalysts. Jaramillo et al. reported a novel strategy to fabricate a unique double-gyroid MoS$_2$ catalyst that preferentially exposes active edge sites, leading to significantly improved

HER activity.[21] Recently, Jin's group developed the metallic 1T-MoS$_2$ catalyst by chemical exfoliation, which exhibits extremely low charge-transfer resistance and thus boosts the HER process.[22] However, to the best of our knowledge, simultaneous optimization of both active sites and conductivity for MoS$_2$ electrocatalysts has not yet been reported, which can be attributed to the contradictory relationship between active sites and conductivity. Apart from the poor intrinsic conductivity in MoS$_2$, abundant active sites are prone to appear with smaller MoS$_2$ nanoparticles or nanodomains, but unfortunately the overall conductivity in such nanostructured materials is hindered due to the poor interparticle or interdomain electron transport and thus reduces the total HER activity. Recently, our group demonstrated the fabrication of defect-rich MoS$_2$ ultrathin nanosheets with additional exposure of active edge sites for HER.[20] Interestingly, the as-formed quasi-periodic arrangement of MoS$_2$ nanodomains partially retains the conductivity along the nanosheets, providing the opportunity for us to optimize the interdomain conductivity of MoS$_2$ catalysts with rich active sites. However, poor intrinsic conductivity of MoS$_2$ still restricts the overall HER activity. Hence, balancing the benefits between rich active sites and good conductivity is the most promising but challenging task for developing efficient HER electrocatalysts.

To overcome this obstacle, we put forward for the first time that elemental incorporation with controllable disorder engineering may realize the synergistic modulations of both active sites and conductivity for efficient HER performance. On one hand, disorder engineering provides the opportunity to tune the number of active sites in HER catalysts, generating more active unsaturated sulfur atoms in more disordered structure. Furthermore, the interdomain conductivity can be modulated by manipulating the 2D electron conjugation, which is related to the degree of disorder.[20] On the other hand, elemental incorporation has been widely used to regulate the electronic structure of semiconductors and thus tune the conductivity of materials,[44−47] giving the opportunity to modulate the intrinsic conductivity of MoS$_2$ electrocatalysts. Molybdenum dioxide (Mo$^{(IV)}$O$_2$) is a classical metallic material with high electric conductivity.[48] Bearing this fact in mind, we propose here that oxygen incorporation in MoS$_2$ may be an effective way to regulate the electronic structure for better intrinsic conductivity. First-principle calculations were carried out to verify our hypothesis. As shown in the calculated density of states (DOS) in Figure 1A, the oxygen-incorporated MoS$_2$ slab possesses much narrower bandgap of 1.30 eV with respect to that of the pristine 2H-MoS$_2$ slab (1.75 eV), indicating that oxygen incorporation in MoS$_2$ ultrathin nanosheets could lead to more charge carriers and higher intrinsic conductivity. Moreover, the bandgap can be further reduced by heavier oxygen incorporation (Supporting Information, SI, Figure S1), thus realizing the controllable electronic modulation. The reduced bandgap can be attributed to the enhanced hybridization between Mo d-orbital and S p-orbital after oxygen incorporation. In order to directly visualize the influence of the electronic structure induced by oxygen incorporation, charge density distributions were investigated. As shown in Figure 1B, the incorporated oxygen atom significantly contributes to the charge density for both valence band and conduction band, which is in sharp contrast to that of the pristine 2H-MoS$_2$ (SI Figure S2), verifying the significant effect of oxygen incorporation on the electronic structure. Moreover, according to the density functional theory (DFT) calculations on the
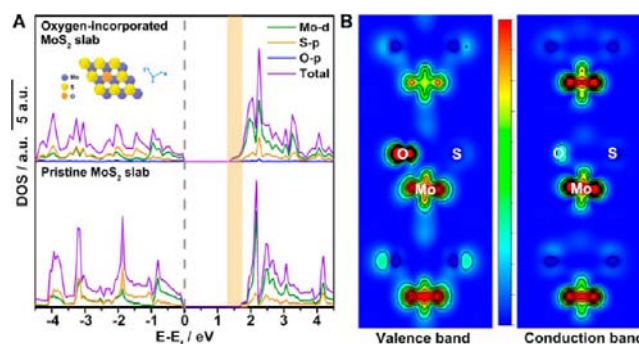
Figure 1. (A) Calculated density of states (DOS) of the oxygen-incorporated MoS$_2$ slab (top) and the pristine 2H-MoS$_2$ slab (bottom). The orange shading clearly indicates the decrease of bandgap after oxygen incorporation. (B) The charge density distributions of valence band (left) and conduction band (right) near the oxygen atom in the oxygen-incorporated MoS$_2$ ultrathin nanosheets, respectively. Black lines represent the contour lines of the charge density.

Gibbs free energy for hydrogen adsorption on the edges of the catalysts (SI S3), the oxygen-incorporated MoS$_2$ slab possesses smaller differential binding free energy than that of the pristine MoS$_2$ system when the H coverage increases from 25% to 50%, indicating a lower energy barrier, or equivalently, a lower overpotential, required to drive the HER process.[39] Of note, much smaller differential binding free energies resulted at higher H coverage for the oxygen-incorporated MoS$_2$ slab (SI Table S1). Hence, higher H coverage can be achieved at lower overpotential for the oxygen-incorporated MoS$_2$ catalyst, providing more effective sites for HER catalysis. Thus, a better HER performance with smaller onset overpotential and larger cathodic current density can be expected. The reduced bandgap, enriched charge density, as well as the small differential binding free energies at high H coverage provide the theoretical support for the high intrinsic conductivity and facile HER process of the oxygen-incorporated MoS$_2$ ultrathin nanosheets. Therefore, simultaneous disorder engineering and oxygen incorporation in MoS$_2$ ultrathin nanosheets would be an effective solution to improve the catalytic activity of HER.

In this work, controllable disorder engineering and oxygen incorporation in MoS$_2$ ultrathin nanosheets are both achieved for the first time, which provide the opportunity for synergistically structural and electronic modulations for HER. Detailed analyses revealed that the number of active unsaturated sulfur atoms can be tuned by disorder engineering, thus realizing the modulation of HER activity in structural aspect. From the viewpoint of electronic modulation, oxygen incorporation can effectively reduce the bandgap and thus enhance the intrinsic conductivity of MoS$_2$ catalyst. Unfortunately, as aforementioned, the key problem that restricts the HER activity is the contradictory relationship between active site numbers and oxygen/disorder codetermined overall conductivity. Herein, we successfully regulated the degree of disorder in the oxygen-incorporated MoS$_2$ ultrathin nanosheets, realizing the balance between active site numbers and overall conductivity for HER catalysis. Benefiting from the controllable disorder engineering and oxygen incorporation, efficient HER activity was achieved for the oxygen-incorporated MoS$_2$ ultrathin nanosheets with a moderate degree of disorder, proving the validity of the combined structural and electronic regulations for improving the electrocatalytic performance. The

success of synergistically structural and electronic modulations in this work will pave a new pathway for pursuing efficient electrocatalysts for energy production and conversion.

■ EXPERIMENTAL SECTION

Materials. All chemicals were purchased from Sinopharm Chemical Reagent Co., Ltd. and used as received.

Synthesis of the Oxygen-Incorporated MoS_2 Ultrathin Nanosheets. Typically, 1 mmol $(NH_4)_6Mo_7O_{24} \cdot 4H_2O$ and 30 mmol thiourea were dissolved in 35 mL distilled water under vigorous stirring to form a homogeneous solution. After being stirred for 30 min, the solution was transferred into a 45 mL Teflon-lined stainless steel autoclave and maintained at different temperatures (i.e., 140–200 °C) for 24 h. Then the reaction system was allowed to cool down to room temperature naturally. The obtained products were collected by centrifugation, washed with distilled water and ethanol, and dried at 60 °C under vacuum.

Characterization. X-ray diffraction (XRD) was performed on a Philips X'Pert Pro Super diffractometer with Cu K_α radiation ($\lambda = 1.54178$ Å). Thermogravimetric analysis (TGA) and differential thermal analysis (DTA) were performed on a SDTQ600 (TA Instruments) TG-DTA Analyzer under the protection of nitrogen. The Fourier transform infrared (FT-IR) spectra were measured on a MAGNA-IR 750 (Nicolet Instrument Co., U.S.). The field emission scanning electron microscopy (FE-SEM) images were taken on a JEOL JSM-6700F SEM. The transmission electron microscopy (TEM) was carried out on a JEM-2100F field emission electron microscope at an acceleration voltage of 200 kV. The high-resolution TEM (HRTEM), high-angle annular dark-field scanning transmission electron microscopy (HAADF-STEM) and corresponding energy-dispersive spectroscopy (EDS) mapping analyses were performed on a JEOL JEM-ARF200F TEM/STEM with a spherical aberration corrector. X-ray photoelectron spectra (XPS) were acquired on an ESCALAB MK II with Mg K_α as the excitation source.

Calculations. The oxygen-incorporated systems, together with the pristine system were handled at the level of density functional theory (DFT) as implemented in the Vienna ab initio Simulation Package (VASP).[49] The periodic boundary conditions with a vacuum space of 15 Å were applied to avoid the interactions between two sheets in nearest-neighbor unit cells. The supercells consisting of $3 \times 3 \times 1$ unit cell for oxygen-incorporated and pristine MoS_2 were selected. The generalized gradient approximation (GGA) was used to account for exchange and correlation in the Perdew−Burke−Ernzerhof form.[50] In our calculations, the single-particle equations were solved by using the projector-augmented wave (PAW) method with a plane-wave cutoff of 500 eV.[51,52] A regular mesh of $6 \times 6 \times 1$ k-points was used to sample the Brillouin zone for the supercells. For the electronic self-consistency loop, a total energy convergence criterion of 1×10^{-5} eV was required. All atomic coordinates were fully optimized until the residual Hellmann−Feynman forces are smaller than 0.01 eV Å^{-1}. The calculation on the Gibbs free energies for hydrogen adsorption on the edges of MoS_2 are according to the literature (SI S3).[39]

Electrochemical Measurements. All of the electrochemical measurements were performed in a three-electrode system on an electrochemical workstation (CHI660B). Typically, 4 mg of catalyst and 30 μL Nafion solution (Sigma Aldrich, 5 wt %) were dispersed in 1 mL water-isopropanol solution with volume ratio of 3:1 by sonicating for 1 h to form a homogeneous ink. Then 5 μL of the dispersion (containing 20 μg of catalyst) was loaded onto a glassy carbon electrode with 3 mm diameter (loading 0.285 mg cm^{-2}). Linear sweep voltammetry with a scan rate of 5 mV s^{-1} was conducted in 0.5 M H_2SO_4 (sparged with pure H_2) using Ag/AgCl (in 3 M KCl solution) electrode as the reference electrode, a graphite rod (Alfa Aesar, 99.9995%) as the counter electrode, and the glassy carbon electrode with various catalysts as the working electrode. All of the potentials were calibrated to a reversible hydrogen electrode (RHE). Cyclic voltammetry (CV) was conducted between −0.3 and 0.2 V vs RHE at 50 mV s^{-1} to investigate the cycling stability. The Nyquist plots were measured with frequencies ranging from 100 kHz to 0.1 Hz

at an overpotential of 250 mV. The impedance data were fitted to a simplified Randles circuit to extract the series and charge-transfer resistances.

■ RESULTS AND DISCUSSION

The oxygen-incorporated MoS_2 ultrathin nanosheets were prepared by controlling the crystallization process. Briefly, lower synthesis temperature is the prerequisite for the formation of oxygen-incorporated MoS_2 ultrathin nanosheets. With decreased synthesis temperature, the reaction process becomes more insufficient, leading to remaining Mo−O bonds inherited from the molybdate precursor, thus realizing the oxygen incorporation. In addition, controllable disorder engineering can also be realized during this process, leading to the formation of oxygen-incorporated MoS_2 ultrathin nanosheets with tunable degrees of disorder. In this work, all of the products are named as SXXX for convenience, where XXX denotes the synthesis temperature in °C. XRD technique was carried out on various samples to investigate the structural information (Figure 2A). As shown in Figure 2A, obvious
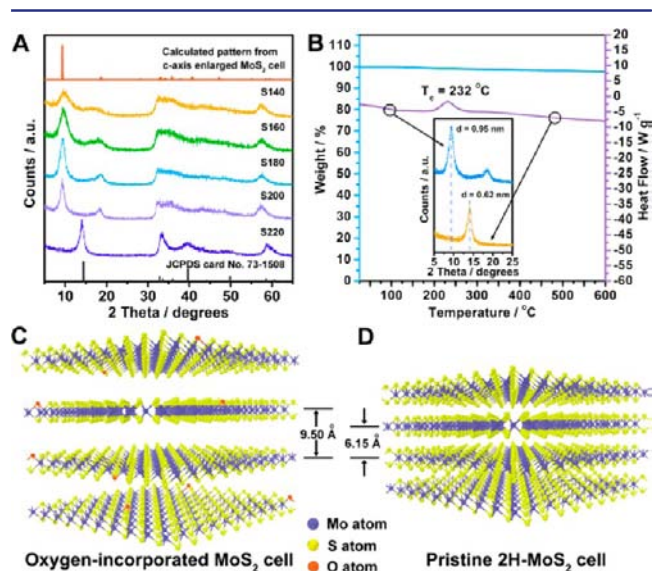

Figure 2. (A) XRD patterns of the products obtained at various temperatures. The standard pattern of the pristine 2H-MoS_2 (JCPDS No.73−1508) and the pattern calculated from the MoS_2 cell with enlarged interlayer spacing are shown as reference. (B) TGA and DTA curves of the oxygen-incorporated MoS_2 ultrathin nanosheets. The inset shows the peak shift of XRD patterns before and after thermal treatment. (C,D) Structural models of (C) the oxygen-incorporated MoS_2 with enlarged interlayer spacing and (D) the pristine 2H-MoS_2.

evolution of XRD patterns can be revealed. At high temperature (220 °C), MoS_2 ultrathin nanosheets with rich defects can be obtained.[20] With the decrease of synthesis temperature, two new peaks emerge at the low-angle region. Detailed analysis of these two peaks shows that the corresponding d spacings are 9.50 Å and 4.75 Å, respectively. The diploid relation between the d spacings clearly indicates the formation of a new lamellar structure with enlarged interlayer spacing of 9.5 Å compared with that of 6.15 Å in pristine 2H-MoS_2 (JCPDS Card No. 73-1508). It is noteworthy that all of the peaks are significantly broadened with decreased synthesis temperature, suggesting the declined crystallinity. Moreover, two broadened peaks at high-angle region (32° and 57°) can be well indexed to (100) and (110) planes of the pristine 2H-MoS_2, indicating the same

atomic arrangement along the basal planes. It is noteworthy that the absence of high-indexed diffraction peaks indicates the short-range disordering nature in the products, which may offer more active sites for HER. To better characterize the product, TGA and DTA measurements are performed. As shown in Figure 2B, negligible weight loss can be observed during the heating process from room temperature to 600 °C, while an obvious endothermal peak emerges at 232 °C. Ex-situ XRD patterns of the sample before and after thermal treatment are shown in the inset of Figure 2B, revealing a structural conversion to the thermodynamically stable 2H-MoS$_2$. Moreover, FT-IR spectra (SI Figure S3) indicate the absence of thiourea molecules in the product. All of the results above reveal that the interlayer spacing enlargement is not the consequence of intercalated molecules, i.e., water or thiourea, between individual MoS$_2$ layers. Combining the results from above analyses, a structural model with enlarged interlayer spacing is constructed (Figure 2C). For direct comparison, a pristine 2H-MoS$_2$ cell with interlayer spacing of 6.15 Å is also presented (Figure 2D). Notably, XRD pattern can be simulated from the as-built structural model with enlarged interlayer spacing (Figure 2A, top), which is consistent with the obtained patterns, revealing the validity of the as-built structural model. Thus, a new lamellar structure with hexagonal MoS$_2$ layers and enlarged interlayer spacing is identified.

FE-SEM and TEM were performed on the as-obtained oxygen-incorporated MoS$_2$ ultrathin nanosheets. Figure 3 outlines that all samples are of ultrathin nanosheet morphology with uniform lateral size in the range of 100−200 nm. From the FE-SEM and TEM images, obvious ripples and corrugations can be observed, revealing the ultrathin nature of the nanosheets.[38] When the synthesis temperature is low (140 or 160 °C), small nanosheets with obscure edges can be obtained, indicating the insufficient crystallization under low-temperature conditions. Oppositely, with increased synthesis temperature, the edges of nanosheets become sharper, suggesting the higher crystallinity of the products. Cross-sectional TEM images (Figure 3A$_3$−D$_3$) of the curled edges of the nanosheets reveal that all products exhibit large interlayer spacing of 9.5 Å, which is consistent with the results from the XRD analysis. The thickness of nanosheets are 5−10 nm, as determined by the cross-sectional TEM images, corresponding to 5−10 sandwiched S−Mo−S layers. Interestingly, accompanied by the decreased synthesis temperature, the fringes of the curled edges become more discontinued, suggesting the decreased crystallinity and increased number of defects.

Controllable disorder engineering was achieved by modulating the reaction process, providing the opportunity to tune the active site numbers. As shown in the HRTEM images (Figure 4), obvious evolution of the degree of disorder with synthesis temperature can be revealed. For S140, the atomic arranging manners on the basal surface are strongly disordered, in which even short-range ordering of nanodomains could not be clearly observed (Figure 4A). With increasing synthesis temperature, small nanodomains with short-range ordering emerged in the manner of quasi-periodic arrangement (Figure 4B,C). The unique quasi-periodic arrangement of nanodomains can partially retain the 2D electron conjugation along the basal surface, leading to fast interdomain electron transport. Interestingly, Moiré patterns can be observed in some parts of the HRTEM image of S180, suggesting the slight rotation between individual MoS$_2$ layers,[53] which is a consequence of the disordered structure. When the synthesis temperature
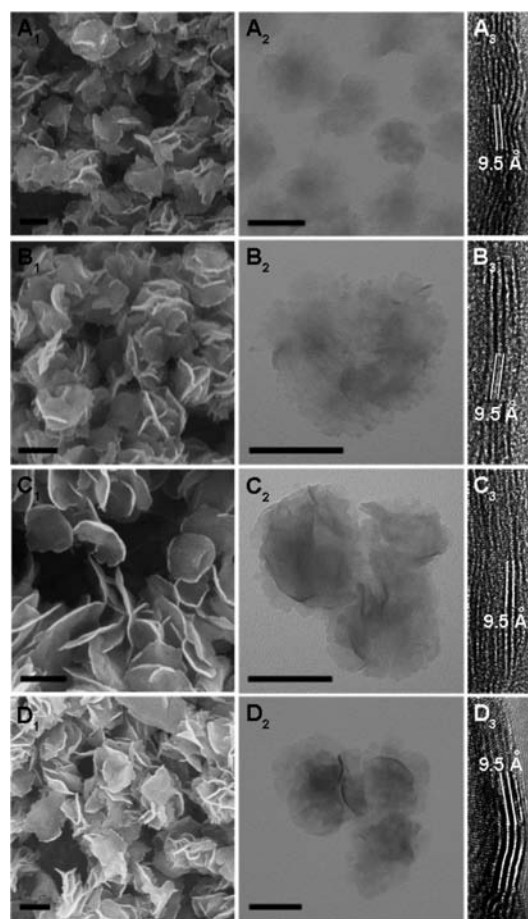
Figure 3. FE-SEM images (A$_1$−D$_1$), TEM images (A$_2$−D$_2$) and cross-sectional TEM images (A$_3$−D$_3$) of the oxygen-incorporated MoS$_2$ ultrathin nanosheets synthesized at various temperatures, where A−D represent for S140, S160, S180, and S200, respectively. All scale bars in FE-SEM and TEM images represent 100 nm.

increases to 200 °C, a more regular atomic arrangement on the basal surface is obtained (Figure 4D). The as-obtained MoS$_2$ nanosheets possess much fewer defects than the nanosheets synthesized at lower temperatures. Hence, the active site numbers may become the limiting factor in HER process. As a result, controllable disorder engineering was realized by simply manipulating the reaction process, providing a platform to investigate the relationship between the structure and HER performance. In order to directly estimate the extent of disorder for various samples, fast Fourier transform (FFT) was applied to the HRTEM images, from which the rotational angles between individual nanodomains can be identified, thus reflecting the degrees of disorder.[54−57] As shown in the insets of Figure 4, the FFT patterns of S140 exhibits a closed diffraction ring, suggesting the strongly disordered arrangement of nanodomains. Meanwhile, S160, S180, and S200 possess six diffraction arcs with different arc length, indicating the quasi-periodic arrangement of nanodomains with different degrees of disorder.[20] The degree of disorder can be evaluated by the angle determined by two end points of a diffraction arc and the central spot. That is, the angle of 60° represents completely disordered atomic arrangement, while 0° represents perfect single crystal without disordering. For convenience, the degrees of disorder for various samples were normalized by 60°, resulting in the relative degree of disorder quantified by
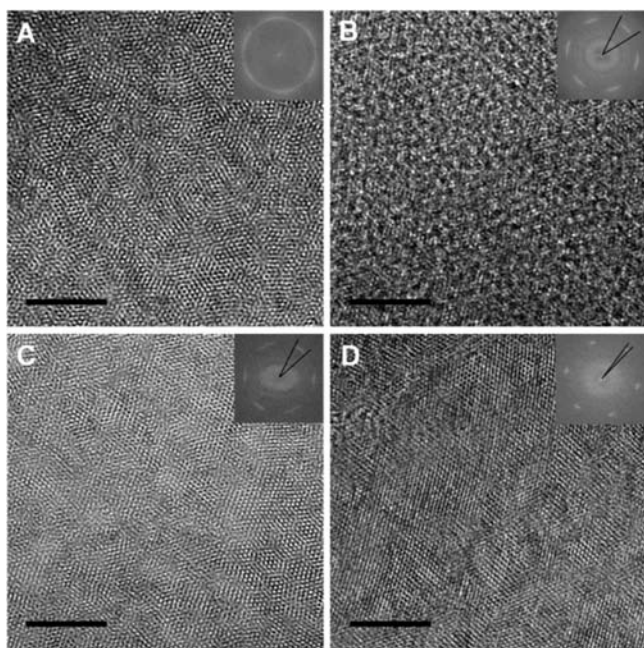
Figure 4. (A−D) HRTEM images and corresponding FFT patterns reveal the controllable disorder engineering with obvious evolution of the degree of disorder. Synthesis temperatures from (A) to (D): 140 °C, 160 °C, 180 °C, and 200 °C, respectively. All scale bars represent 5 nm.

Table 1. Degrees of Disorder and Elemental Analyses of the Oxygen-Incorporated MoS$_2$ Ultrathin Nanosheets

			atomic ratio of Mo/S	
	degree of disorder	atom% of oxygen	by XPS	by EDS
S140	100%	4.18	1:2.10	1:2.10
S160	53.3−56.7%	3.36	1:2.07	1:2.09
S180	35.0−40.0%	2.28	1:2.04	1:2.05
S200	8.3−13.3%	1.92	1:2.02	1:2.01

percentage (Table 1). Thus, a clear evolution of the degree of disorder with synthesis temperature was revealed. In detail, S140 possesses the highest degree of disorder of 100%, while the S160, S180, and S200 exhibit degrees of disorder of 53.3−56.7%, 35.0−40.0%, and 8.3−13.3%, respectively. To the best of our knowledge, it is the first time to realize controllable disorder engineering in metal chalcogenides. From the structural viewpoint for HER catalysis, although the strongly disordered structure can provide more accessible active atoms as active sites,[58,59] the electron transport along the basal surfaces is significantly blocked due to the collapse of 2D electron conjugation[20] and thus lead to poor overall conductivity and further restrict the HER process. Hence, quasi-periodic structures with a moderate degree of disorder should be beneficial for HER, since the contradictory relation between active sites and conductivity may reach a balance. Therefore, optimizing the degree of disorder with the simultaneous consideration of intrinsic conductivity of the MoS$_2$ nanodomains is crucial for improving the HER performance.

As proven by calculations, oxygen incorporation is an effective solution to enhance the intrinsic conductivity of MoS$_2$ catalysts. In order to investigate the chemical composition of the products, XPS and elemental mapping analyses were carried out. As shown in Figure 5A, two
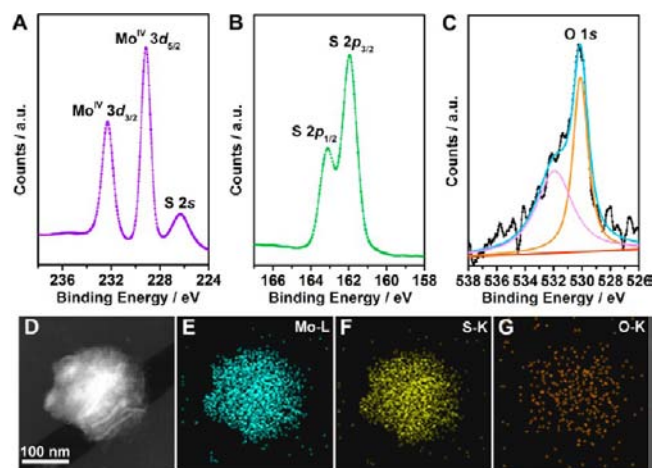
Figure 5. (A−C) XPS spectra showing the binding energies of molybdenum, sulfur, and oxygen. (D−G) HAADF-STEM image and corresponding EDS mapping images of an individual oxygen-incorporated MoS$_2$ ultrathin nanosheet, indicating the homogeneous distribution of molybdenum, sulfur, and oxygen.

characteristic peaks arising from Mo 3d$_{5/2}$ and Mo 3d$_{3/2}$ orbitals are located at 229.1 and 232.1 eV, suggesting the dominance of Mo$^{(IV)}$ in the product.[21] Whereas the S 2p region (Figure 5B) exhibits primarily a single doublet with the 2p$_{3/2}$ peak at 161.8 eV, which is consistent with −2 oxidation state of sulfur.[21] Detailed compositional analysis (Table 1) reveals that the atomic ratio of Mo:S varies from 1:2.02 to 1:2.10 as the synthesis temperature decreases, giving the direct evidence that the number of unsaturated sulfur atoms is dependent on the degree of disorder. Furthermore, the oxygen incorporation in MoS$_2$ was verified. As shown in Figure 5C, the O 1s peak located at 530.0 eV is corresponding to the binding energy of oxygen in Mo$^{(IV)}$O$_2$,[60] suggesting the existence of Mo$^{(IV)}$−O bonds, thus verifying the successful oxygen incorporation rather than the surface oxidation. The peak located at 532.0 eV can be attributed to adsorbed water. Moreover, Raman spectra of the product verified the existence of Mo−O bonds combined with the MoS$_2$ structure (SI Figure S4). Furthermore, the HAADF-STEM image and corresponding EDS mapping analyses (Figure 5D−G) reveal the homogeneous distribution of molybdenum, sulfur, and oxygen in the whole ultrathin nanosheet. All of the results above prove the successful oxygen incorporation in MoS$_2$ ultrathin nanosheets. As verified by DFT calculations, oxygen incorporation could effectively regulate the electronic structure of MoS$_2$, leading to the enhancement of intrinsic conductivity, which should be beneficial for HER. Therefore, from the above analyses, efficient HER activity can be expected for the oxygen-incorporated MoS$_2$ ultrathin nanosheets with a moderate degree of disorder.

In order to verify our expectation, electrochemical measurements (Figure 6) of the oxygen-incorporated MoS$_2$ ultrathin nanosheets with different degrees of disorder as well as the bulk MoS$_2$ were performed to investigate the HER activity. All measurements were carried out at the same optimized loading weight of 0.285 mg cm^{-2}. As shown in Figure 6A, all of the oxygen-incorporated MoS$_2$ catalysts possess much lower onset overpotentials (η) than the bulk MoS$_2$, among all S180 exhibits the lowest value of 120 mV, suggesting the superior HER activity. Cathodic current density is considered as an important evaluating criterion for HER activity. As shown in Figure 6A, S180 exhibits an extremely large cathodic current density of
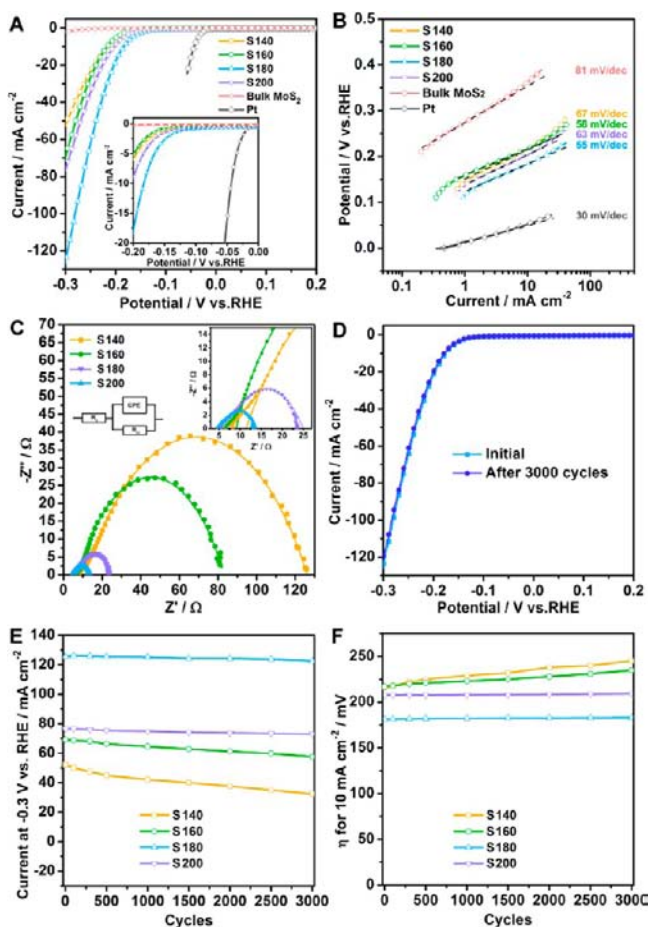
Figure 6. (A) Polarization curves and (B) corresponding Tafel plots of the oxygen-incorporated MoS_2 ultrathin nanosheets. Inset: enlargement of the region near the onset. (C) Nyquist plots of different samples. The fitted curves are presented by solid lines. (D) Polarization curves revealing that negligible degradation of HER activity is observed for S180 even after 3000 CV cycles. (E) Cycling stability of various catalysts at overpotential of 300 mV. (F) The overpotential required to drive 10 mA cm^{-2} in dependence of cycle numbers for various electrocatalysts.

126.5 mA cm^{-2} at η = 300 mV, which is 60 times larger than the current observed in bulk MoS_2 and larger compared to the other three synthesized materials (52−77 mA cm^{-2}). Notably, the cathodic current density of 126.5 mA cm^{-2} for S180 is among the best results for single-component MoS_2 electrocatalysts, suggesting the superior HER activity of the optimized catalyst. Moreover, the corresponding Tafel plots (Figure 6B) indicate that the products with moderately disordered structure (S180 and S160) possess smaller Tafel slopes (55 and 58 mV decade^{-1}) than the strongly disordered catalyst (67 mV decade^{-1} for S140) and less disordered catalyst (63 mV decade^{-1} for S200). The as-obtained Tafel slope of 55 mV decade^{-1} for S180 is among the lowest records for single-component MoS_2 electrocatalysts.[20−23]

Three principle steps for converting H$^+$ to H$_2$ have been proposed for HER in acidic medium.[61,62] The first is a primary discharge step (i.e., Volmer reaction, eq 1):

$$H_3O^+ + e^- \rightarrow H_{ads} + H_2O \tag{1}$$

Followed by the primary discharge step, the electrochemical desorption step (i.e., Heyrovsky reaction, eq 2) or recombination step (i.e., Tafel reaction, eq 3) may be involved:

$$H_{ads} + H_3O^+ + e^- \rightarrow H_2 + H_2O \tag{2}$$

$$H_{ads} + H_{ads} \rightarrow H_2 \tag{3}$$
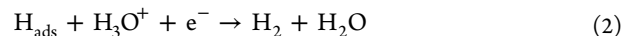
Tafel slope is an inherent property of electrocatalysts that is determined by the rate-limiting step of HER. Under a specific set of conditions, when the Volmer reaction is the rate-limiting step of HER, a slope of 120 mV decade^{-1} should be observed, whereas if Heyrovsky or Tafel reactions act as the rate-limiting step, Tafel slopes of 30 and 40 mV decade^{-1} can be obtained, respectively.[61,62] For a complete HER process, combinations of steps, i.e., Volmer-Heyrovsky or Volmer-Tafel mechanism, should be involved to produce molecular hydrogen. Although the HER mechanism for MoS_2 still remains inconclusive due to the reaction complexity, the Tafel slope of 55 mV decade^{-1} in this work is indeed close to the values of the defect-rich MoS_2 ultrathin nanosheets[20] and the MoS_2 nanoplates synthesized in ultrahigh vacuum,[23] suggesting the similar surface chemistry of the oxygen-incorporated MoS_2 ultrathin nanosheets. It is believed that the small Tafel slope will be beneficial in practical applications, because it will lead to a strongly enhanced HER rate at a moderate increase of overpotential.[8]

By applying extrapolation method to the Tafel plots, exchange current densities are obtained (SI Figure S5 and Table 2). As shown in Table 2, S180 exhibits remarkable

Table 2. Electrochemical Parameters of the Oxygen-Incorporated MoS_2 Ultrathin Nanosheets

	exchange current density, $j_0/\mu A\ cm^{-2}$	double-layer capacitance, $C_{dl}/\mu F$	charge-transfer resistance, R_{ct}/Ω	series resistance, R_s/Ω
S140	5.6	3.2	124.6	8.7
S160	2.8	10.8	78.9	7.1
S180	12.6	37.7	8.8	4.7
S200	6.3	11.7	19.0	6.8

exchange current density (j_0) of 12.6 μA cm^{-2}, which is 2−4.5 times larger than the values obtained for the other three counterparts and almost 40 times larger than the value of bulk MoS_2, suggesting the excellent activity for HER catalysis. The large j_0 can be attributed to the moderate degree of disorder and ultrathin nanosheet morphology that can offer more effective active sites.[15] Furthermore, electrochemical double-layer capacitances (C_{dl}) are measured to evaluate the effective surface area of various catalysts (SI Figure S6). As shown in Table 2, S180 exhibits much larger C_{dl} of 37.7 μF than the other counterparts, indicating the high exposure of effective active sites, which is responsible for the excellent HER activity.[22]

To prove the better balance between intrinsic and interdomain conductivity for S180, the electrochemical impedance spectroscopy (EIS) is performed to investigate the electrode kinetics under HER process (Figure 6C). The Nyquist plots reveal a remarkable decrease of the charge-transfer resistance (R_{CT}) from 124.6 Ω (S140) to 8.8 Ω (S180), which can be attributed to the enhancement of interdomain conductivity with decreased degree of disorder (Table 2). Moreover, the R_{CT} of S180 is smaller than the value of S200, which may arise from the heavier oxygen incorporation in S180 that enhances the intrinsic conductivity. As a result, S180

17886

dx.doi.org/10.1021/ja408329q | J. Am. Chem. Soc. 2013, 135, 17881−17888

possesses both rich effective active sites and high overall conductivity, which determine the superior HER activity, suggesting the achievement of synergistically structural and electronic modulations for HER catalysis.

Besides the HER activity, stability is another significant criterion to evaluate an advanced electrocatalyst. To investigate the stability in acidic environment, long-term cycling stability of S180 is investigated by performing continuous cyclic voltammetry (CV) between −0.3 and 0.2 V vs RHE at 50 mV s⁻¹. As shown in Figure 6D, negligible difference can be observed between the curves measured at the initial cycle and after 3000 CV cycles, suggesting the excellent durability of S180 during long-term cycling. When a constant overpotential of 300 mV is applied, a continuous HER process occurs to generate molecular hydrogen. As shown in SI Figure S8, the current density exhibits only slight degradation even after a long period of 20 000 s, which might be caused by the consumption of H⁺ or the accumulation of H₂ bubbles on the electrode surface that hinder the reaction.[20] Thus, the stability under continuous HER process is identified for S180. The fair comparison of stability between the oxygen-incorporated MoS₂ ultrathin nanosheets with different degrees of disorder is shown in Figure 6E−F in two manners: as plots of (E) current density at η = 300 mV and (F) overpotential required for obvious hydrogen evolution (10 mA cm⁻²) versus the cycling numbers. It can be seen that negligible degradations are observed for S180 and S200 for both current and potential cycling up to 3000 cycles, suggesting the superior stability of the high-temperature products. In sharp contrast, S140 and S160 possess rather poor long-term stability, which can be attributed to the relatively large solubility in acidic medium owing to the poor crystallinity.[20] The good chemical stability of S180 is also demonstrated (SI Figure S9), suggesting that only slight degradation of HER activity happens even after six-month storage under air atmosphere. All of the results above prove that S180 possesses superior HER activity as well as excellent stability, making it a promising HER catalyst for practical applications.

The high HER activity as well as good stability of the optimized catalyst with synergistically structural and electronic modulations can be attributed to four aspects as follows: (i) the disordered structure offers large amounts of unsaturated sulfur atoms as active sites for hydrogen evolution catalysis (Figure 7A); (ii) the moderate degree of disorder provides quasi-periodic arrangement of nanodomains, which partially retains the 2D electron conjugation, leading to fast interdomain electron transport (Figure 7A); (iii) the oxygen incorporation in MoS₂ reduces the bandgap, thus enhances the intrinsic conductivity of nanodomains and facilitates the combination between positive protons and catalyst (Figure 7B); (iv) the relatively high crystallinity of moderately disordered catalyst ensures the stability during long-term electrocatalysis. In general, integrated optimization of MoS₂ electrocatalyst by structural and electronic modulations was realized for efficient electrocatalytic hydrogen evolution, and the combined modulations of active sites and conductivity may pave a new pathway for improving the activity of various electrocatalysts.

CONCLUSIONS

In summary, controllable disorder engineering and oxygen incorporation were achieved in MoS₂ ultrathin nanosheets for the first time, providing the opportunity to synergistically modulate both structural and electronic benefits for hydrogen
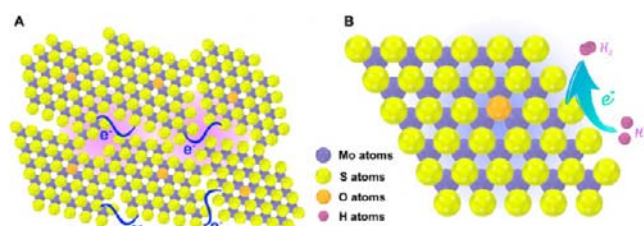
Figure 7. (A) Schematic representation of the disordered structure in oxygen-incorporated MoS₂ ultrathin nanosheets. The blue lines represent the fast electron transport between the quasi-periodically aligned nanodomains; the purple shadings indicate the enrichment effect of active sites arising from the disordered structure. (B) Constructed model of an individual oxygen-incorporated MoS₂ nanodomain and the illustration of the HER process at the active sites. The blue shading represents the enhanced charge density induced by the incorporated oxygen atom which improves the intrinsic conductivity and facilitates the combination between catalyst and positive protons.

evolution. In this work, two key factors that affect the HER performance, the number of active sites and conductivity, were synergistically regulated. As the degree of disorder increases, more unsaturated sulfur atoms are generated as active sites for HER catalysis, while the interdomain conductivity is restricted due to the damage of 2D electron conjugation along the strongly disordered MoS₂ nanosheets. Meanwhile, oxygen incorporation effectively reduces the bandgap of MoS₂ catalyst, leading to the enhancement of the intrinsic conductivity. Thus, by modulating the degrees of disorder, the optimized oxygen-incorporated MoS₂ catalyst with a moderate degree of disorder was identified, which possesses both rich active sites and high overall conductivity, exhibiting superior HER performance. As a result, the optimized catalyst exhibits remarkable HER activity with a large cathodic current density of 126.5 mA cm⁻² at an overpotential of 300 mV. Moreover, a low onset overpotential of 120 mV, a small Tafel slope of 55 mV decade⁻¹, as well as excellent long-term stability are all achieved, making the optimized oxygen-incorporated MoS₂ catalyst a prominent alternative for platinum-based HER electrocatalysts. This work will broaden our vision to improve the activity of various electrocatalysts by synergistically structural and electronic modulations.

ASSOCIATED CONTENT

Ⓢ Supporting Information
Supplementary calculations of the oxygen-incorporated MoS₂ ultrathin nanosheets and pristine MoS₂, FT-IR spectra, Raman spectra, exchange current densities, double-layer capacitance measurements, and additional stability tests. This material is available free of charge via the Internet at http://pubs.acs.org.

AUTHOR INFORMATION

Corresponding Author
yxie@ustc.edu.cn
Notes
The authors declare no competing financial interest.

ACKNOWLEDGMENTS

■ REFERENCES

(1) Mallouk, T. E. *Nat. Chem.* **2013**, *5*, 362.

(2) Turner, J. A. *Science* **2004**, *305*, 972.

(3) Norskov, J. K.; Christensen, C. H. *Science* **2006**, *312*, 1322.

(4) Greeley, J.; Jaramillo, T. F.; Bonde, J.; Chorkendorff, I.; Norskov, J. K. *Nat. Mater.* **2006**, *5*, 909.

(5) Casado-Rivera, E.; Volpe, D. J.; Alden, L.; Lind, C.; Downie, C.; Vázquez-Alvarez, T.; Angelo, A. C. D.; DiSalvo, F. J.; Abruña, H. D. *J. Am. Chem. Soc.* **2004**, *126*, 4043.

(6) Voiry, D.; Yamaguchi, H.; Li, J.; Silva, R.; Alves, D. C. B.; Fujita, T.; Chen, M.; Asefa, T.; Shenoy, V. B.; Eda, G.; Chhowalla, M. *Nat. Mater.* **2013**, *12*, 850.

(7) Merki, D.; Fierro, S.; Vrubel, H.; Hu, X. *Chem. Sci.* **2011**, *2*, 1262.

(8) Merki, D.; Hu, X. *Energy Environ. Sci.* **2011**, *4*, 3878.

(9) Vrubel, H.; Merki, D.; Hu, X. *Energy Environ. Sci.* **2012**, *5*, 6136.

(10) Kim, J.; Byun, S.; Smith, A. J.; Yu, J.; Huang, J. *J. Phys. Chem. Lett.* **2013**, *4*, 1227.

(11) Kong, D.; Wang, H.; Cha, J. J.; Pasta, M.; Koski, K. J.; Yao, J.; Cui, Y. *Nano Lett.* **2013**, *13*, 1341.

(12) Gao, M.-R.; Lin, Z.-Y.; Zhuang, T.-T.; Jiang, J.; Xu, Y.-F.; Zheng, Y.-R.; Yu, S.-H. *J. Mater. Chem.* **2012**, *22*, 13662.

(13) Vrubel, H.; Hu, X. *Angew. Chem., Int. Ed.* **2012**, *51*, 12703.

(14) Chen, W. F.; Wang, C. H.; Sasaki, K.; Marinkovic, N.; Xu, W.; Muckerman, J. T.; Zhu, Y.; Adzic, R. R. *Energy Environ. Sci.* **2013**, *6*, 943.

(15) Chen, W.-F.; Sasaki, K.; Ma, C.; Frenkel, A. I.; Marinkovic, N.; Muckerman, J. T.; Zhu, Y.; Adzic, R. R. *Angew. Chem., Int. Ed.* **2012**, *51*, 6131.

(16) Popczun, E. J.; McKone, J. R.; Read, C. G.; Biacchi, A. J.; Wiltrout, A. M.; Lewis, N. S.; Schaak, R. E. *J. Am. Chem. Soc.* **2013**, *135*, 9267.

(17) Hu, X.; Brunschwig, B. S.; Peters, J. C. *J. Am. Chem. Soc.* **2007**, *129*, 8988.

(18) Jacques, P.-A.; Artero, V.; Pécaut, J.; Fontecave, M. *Proc. Natl. Acad. Sci. U.S.A.* **2009**, *106*, 20627.

(19) Andreiadis, E. S.; Jacques, P.-A.; Tran, P. D.; Leyris, A.; Chavarot-Kerlidou, M.; Jousselme, B.; Matheron, M.; Pécaut, J.; Palacin, S.; Fontecave, M.; Artero, V. *Nat. Chem.* **2013**, *5*, 48.

(20) Xie, J.; Zhang, H.; Li, S.; Wang, R.; Sun, X.; Zhou, M.; Zhou, J.; Lou, X. W.; Xie, Y. *Adv. Mater.* **2013**, *25*, 5807.

(21) Kibsgaard, J.; Chen, Z.; Reinecke, B. N.; Jaramillo, T. F. *Nat. Mater.* **2012**, *11*, 963.

(22) Lukowski, M. A.; Daniel, A. S.; Meng, F.; Forticaux, A.; Li, L.; Jin, S. *J. Am. Chem. Soc.* **2013**, *135*, 10274.

(23) Jaramillo, T. F.; Jørgensen, K. P.; Bonde, J.; Nielsen, J. H.; Horch, S.; Chorkendorff, I. *Science* **2007**, *317*, 100.

(24) Chen, Z.; Cummins, D.; Reinecke, B. N.; Clark, E.; Sunkara, M. K.; Jaramillo, T. F. *Nano Lett.* **2011**, *11*, 4168.

(25) Wang, T.; Liu, L.; Zhu, Z.; Papakonstantinou, P.; Hu, J.; Liu, H.; Li, M. *Energy Environ. Sci.* **2013**, *6*, 625.

(26) Hou, Y.; Laursen, A. B.; Zhang, J.; Zhang, G.; Zhu, Y.; Wang, X.; Dahl, S.; Chorkendorff, I. *Angew. Chem., Int. Ed.* **2013**, *52*, 3621.

(27) Meng, F.; Li, J.; Cushing, S. K.; Zhi, M.; Wu, N. *J. Am. Chem. Soc.* **2013**, *135*, 10286.

(28) Chang, Y.-H.; Lin, C.-T.; Chen, T.-Y.; Hsu, C.-L.; Lee, Y.-H.; Zhang, W.; Wei, K.-H.; Li, L.-J. *Adv. Mater.* **2013**, *25*, 756.

(29) Benck, J. D.; Chen, Z.; Kuritzky, L. Y.; Forman, A. J.; Jaramillo, T. F. *ACS Catal.* **2012**, *2*, 1916.

(30) Laursen, A. B.; Vesborg, P. C. K.; Chorkendorff, I. *Chem. Commun.* **2013**, *49*, 4965.

(31) Karunadasa, H. I.; Montalvo, E.; Sun, Y.; Majda, M.; Long, J. R.; Chang, C. J. *Science* **2012**, *335*, 698.

(32) Xu, M.; Liang, T.; Shi, M.; Chen, H. *Chem. Rev.* **2013**, *113*, 3766.

(33) Huang, X.; Zeng, Z.; Zhang, H. *Chem. Soc. Rev.* **2013**, *42*, 1934.

(34) Wang, Q. H.; Kalantar-Zadeh, K.; Kis, A.; Coleman, J. N.; Strano, M. S. *Nat. Nanotechnol.* **2012**, *7*, 699.

(35) Chhowalla, M.; Shin, H. S.; Eda, G.; Li, L.-J.; Loh, K. P.; Zhang, H. *Nat. Chem.* **2013**, *5*, 263.

(36) Zhang, X.; Xie, Y. *Chem. Soc. Rev.* **2013**, *42*, 8187.

(37) Feng, J.; Sun, X.; Wu, C.; Peng, L.; Lin, C.; Hu, S.; Yang, J.; Xie, Y. *J. Am. Chem. Soc.* **2011**, *133*, 17832.

(38) Xie, J.; Sun, X.; Zhang, N.; Xu, K.; Zhou, M.; Xie, Y. *Nano Energy* **2013**, *2*, 65.

(39) Hinnemann, B.; Moses, P. G.; Bonde, J.; Jørgensen, K. P.; Nielsen, J. H.; Horch, S.; Chorkendorff, I.; Nørskov, J. K. *J. Am. Chem. Soc.* **2005**, *127*, 5308.

(40) Li, Y.; Wang, H.; Xie, L.; Liang, Y.; Hong, G.; Dai, H. *J. Am. Chem. Soc.* **2011**, *133*, 7296.

(41) Liang, Y.; Li, Y.; Wang, H.; Dai, H. *J. Am. Chem. Soc.* **2013**, *135*, 2013.

(42) Liao, L.; Zhu, J.; Bian, X.; Zhu, L.; Scanlon, M. D.; Girault, H. H.; Liu, B. *Adv. Funct. Mater.* **2013**, *23*, 5326.

(43) Wu, Z.-S.; Yang, S.; Sun, Y.; Parvez, K.; Feng, X.; Müllen, K. *J. Am. Chem. Soc.* **2012**, *134*, 9082.

(44) Schulthess, T. C.; Temmerman, W. M.; Szotek, Z.; Butler, W. H.; Malcolm Stocks, G. *Nat. Mater.* **2005**, *4*, 838.

(45) Mocatta, D.; Cohen, G.; Schattner, J.; Millo, O.; Rabani, E.; Banin, U. *Science* **2011**, *332*, 77.

(46) Wu, C.; Feng, F.; Feng, J.; Dai, J.; Peng, L.; Zhao, J.; Yang, J.; Si, C.; Wu, Z.; Xie, Y. *J. Am. Chem. Soc.* **2011**, *133*, 13798.

(47) Lin, C.; Zhu, X.; Feng, J.; Wu, C.; Hu, S.; Peng, J.; Guo, Y.; Peng, L.; Zhao, J.; Huang, J.; Yang, J.; Xie, Y. *J. Am. Chem. Soc.* **2013**, *135*, 5144.

(48) Hu, B.; Mai, L.; Chen, W.; Yang, F. *ACS Nano* **2009**, *3*, 478.

(49) Kresse, G.; Furthmüller, J. *Phys. Rev. B* **1996**, *54*, 11169.

(50) Perdew, J. P.; Burke, K.; Ernzerhof, M. *Phys. Rev. Lett.* **1996**, *77*, 3865.

(51) Kresse, G.; Joubert, D. *Phys. Rev. B* **1999**, *59*, 1758.

(52) Blöchl, P. E. *Phys. Rev. B* **1994**, *50*, 17953.

(53) Najmaei, S.; Liu, Z.; Zhou, W.; Zou, X.; Shi, G.; Lei, S.; Yakobson, B. I.; Idrobo, J.-C.; Ajayan, P. M.; Lou, J. *Nat. Mater.* **2013**, *12*, 754.

(54) Kim, K.; Lee, Z.; Regan, W.; Kisielowski, C.; Crommie, M. F.; Zettl, A. *ACS Nano* **2011**, *5*, 2142.

(55) Huang, P. Y.; Ruiz-Vargas, C. S.; van der Zande, A. M.; Whitney, W. S.; Levendorf, M. P.; Kevek, J. W.; Garg, S.; Alden, J. S.; Hustedt, C. J.; Zhu, Y.; Park, J.; McEuen, P. L.; Muller, D. A. *Nature* **2011**, *469*, 389.

(56) Gibb, A. L.; Alem, N.; Chen, J.-H.; Erickson, K. J.; Ciston, J.; Gautam, A.; Linck, M.; Zettl, A. *J. Am. Chem. Soc.* **2013**, *135*, 6758.

(57) An, J.; Voelkl, E.; Suk, J. W.; Li, X.; Magnuson, C. W.; Fu, L.; Tiemeijer, P.; Bischoff, M.; Freitag, B.; Popova, E.; Ruoff, R. S. *ACS Nano* **2011**, *5*, 2433.

(58) Van Swygenhoven, H. *Science* **2002**, *296*, 66.

(59) Xie, J.; Wu, C.; Hu, S.; Dai, J.; Zhang, N.; Feng, J.; Yang, J.; Xie, Y. *Phys. Chem. Chem. Phys.* **2012**, *14*, 4810.

(60) Sun, Y.; Hu, X.; Luo, W.; Huang, Y. *ACS Nano* **2011**, *5*, 7100.

(61) Pentland, N.; Bockris, J. O. M.; Sheldon, E. *J. Electrochem. Soc.* **1957**, *104*, 182.

(62) Conway, B. E.; Tilak, B. V. *Electrochim. Acta* **2002**, *47*, 3571.